An Extreme Weather Risk-averse Planning Method for Soft Open Points Considering Distribution Network Reconfiguration

Zhuoxu Chen, Zechun Hu, Yujian Wan, and Junsong Li

***Abstract*—Extreme weather conditions, characterized as high-impact low-probability (HILP) events, pose significant threats to distribution network (DN). Soft open points (SOPs) have emerged for precise power flow regulation and voltage establishment, and hence can be used for post-fault load restoration to improve the DN resilience, incorporating scenarios generated from weather profiles. In this paper, an extreme weather risk-averse planning method for SOPs is proposed. A two-stage scenario-based stochastic programming (SBSP) model is established to minimize expectation and conditional value-at-risk (CVaR) of load shedding and network loss. Due to the integer variables introduced by DN reconfiguration constraints in the operational stage, the classic Benders decomposition algorithm is inapplicable. To address this challenge, we develop a novel generalized Benders decomposition (GBD)-based solution algorithm, designed to improve the computational efficiency on large-scale cases. Lift-and-project (L&P) cutting plane is employed to derive Benders cuts through the convex hull of mixed-integer second-order cone programming (MISOCP) subproblems. Finally, the effectiveness of the proposed method is demonstrated by numerical experiences on 33- and 123-node test DNs.**

***Index Terms*—Resilience, soft open point (SOP), extreme weather, distribution network, network reconfiguration, Benders decomposition.**

NOMENCLATURE

A. Mathematical Operators

$\lvert\cdot\rvert$	Absolute value or dimension of a set
$[\cdot]_+$	The maximum value between variable and 0
$\lVert\cdot\rVert_2$	2-norm of a vector
$\nabla[\cdot]$	Gradient of a vector

Manuscript received: February 17, 2025; revised: June 5, 2025; accepted: September 28, 2025. Date of CrossCheck: September 28, 2025. Date of online publication: October 17, 2025.

This work was supported by the Technology Project of China Southern Power Grid (No. 030500KK52220004).

This article is distributed under the terms of the Creative Commons Attribution 4.0 International License (http://creativecommons.org/licenses/by/4.0/).

Z. Chen and Z. Hu (corresponding author) are with the Department of Electrical Engineering, Tsinghua University, Beijing, China (e-mail: chenzx22@mails.tsinghua.edu.cn; zechhu@tsinghua.edu.cn).

Y. Wan and J. Li are with the Shantou Power Supply Bureau of Guangdong Power Grid Corporation, Shantou, China (e-mail: 5377151@qq.com; 541341266@qq.com).

DOI: 10.35833/MPCE.2025.000131

B. Sets and Indices

ω, Ω	Index and set of scenarios
$\mathcal{B}_{\omega}^{\text{out}}$	Set of outage branches in scenario ω
i, j	Indices of nodes
$\mathcal{I}_1$, $\mathcal{I}_2$	Sets of index variables in the first and second stages
k	Index of Benders iterations
$\mathcal{N}$, $\mathcal{B}$	Sets of nodes and branches
$\mathcal{N}_{\omega}^{\text{iso}}$, $\mathcal{B}_{\omega}^{\text{iso}}$	Sets of completely isolated nodes and branches in scenario ω
$\mathcal{N}^{\text{sop}}$, $\mathcal{B}^{\text{sop}}$	Set of candidate soft open point (SOP) nodes and branches

C. Parameters

α	Confidence level of conditional value-at-risk (CVaR)
μ	Risk aversion coefficient
π^{crf}	Capital recovery factor
π_i^{dg}	Generation cost of distributed generator (DG) at node i
π^{ls}	Load shedding penalty
π_{ω}^{mg}	Electricity price in scenario ω
π^{nl}	Network loss cost
σ_i, σ_j	Loss rates of voltage source converters (VSCs) on terminals i and j of SOP (i,j)
θ_i^{dg}	Power factor angle of DG at node i
$\boldsymbol{A}_{l,\omega}$, $\boldsymbol{b}_{l,\omega}$, $\boldsymbol{c}_{l,\omega}$, $\boldsymbol{d}_{l,\omega}$	Coefficient matrix and vectors related to the l^{th} second-order cone programming (SOCP) constraint
a_{ij}^0	Initial status of branch (i,j)
$f_{ij}^{\text{sop,fi}}$, $f_{ij}^{\text{sop,va}}$	Fixed and variable investment costs of SOP (i,j)
$I_{\max}$	Upper bound of branch current
m	Maintenance cost factor of SOP
M	Sufficiently large positive number
p_{ω}	Probability of scenario ω
$p_{\text{fail}}(s)$	Failure probability with respect to weather intensity s

p_{nm} Inherent failure probability under normal conditions

$P_{i,\omega}^{\mathrm{d}}$, $Q_{i,\omega}^{\mathrm{d}}$ Active and reactive load demands at node i in scenario ω

$P_{\max}^{\mathrm{mg}}$, $Q_{\max}^{\mathrm{mg}}$ The maximum active and reactive power injected from main grid

r Discount rate

R_{ij}, X_{ij} Resistance and reactance of branch (i,j)

s Weather intensity

s_{co} Collapse intensity of a distribution line

s_{cr} Critical intensity of a distribution line

$S_{\max}^{\mathrm{sop}}$, $S_{\min}^{\mathrm{sop}}$ Upper and lower bounds of SOP capacity

T Planning horizon

$U_{\max}$, $U_{\min}$ Upper and lower bounds of nodal voltage

w_i Priority weight of load at node i

D. Variables

η Continuous value-at-risk of planning scheme

$\lambda_{i,\omega}$ Continuous restoration rate of load demand at node i in scenario ω, $\lambda_{i,\omega} \in [0,1]$

$a_{ij,\omega}$ Binary variable that equals to 1 if branch (i,j) is connected in scenario ω, and 0 otherwise

$b_{ij,\omega}$ Continuous variable that equals to 1 if direction of branch (i,j) points from i to j in scenario ω, and 0 otherwise

C^{inv} Annual investment cost

$C_{\omega}^{\mathrm{ope}}$ Operational cost in scenario ω

$C_{\omega}^{\mathrm{risk}}$ Risk cost in scenario ω

$CVaR_{\alpha}$ CVaR under confidence level α

$I_{ij,\omega}^{\mathrm{sq}}$ Continuous square of current on branch (i,j) in scenario ω

$P_{ij,\omega}$, $Q_{ij,\omega}$ Continuous active and reactive power flows on branch (i,j) in scenario ω

$P_{i,\omega}^{\mathrm{dg}}$, $Q_{ij,\omega}^{\mathrm{dg}}$ Continuous active and reactive generations of DG at node i in scenario ω

$P_{i,\omega}^{\mathrm{mg}}$, $Q_{ij,\omega}^{\mathrm{mg}}$ Continuous active and reactive power injections at node i from main grid in scenario ω

$P_{i,\omega}^{\mathrm{sop}}$, $Q_{ij,\omega}^{\mathrm{sop}}$ Continuous active and reactive power injections of SOP at node i in scenario ω

S_{ij}^{sop} Continuous construction capacity of SOP on branch (i,j)

$U_{i,\omega}^{\mathrm{sq}}$ Continuous square of voltage magnitude at node i in scenario ω

x_{ij}^{sop} Binary variable that equals to 1 if an SOP is installed on branch (i,j), and 0 otherwise

$\boldsymbol{X}$ Vector of first-stage variables

$\boldsymbol{Y}_{\omega}$ Vector of second-stage variables in scenario ω

$z_{i,\omega}$ Binary variable that equals 1 if node i acts as a root node in scenario ω, and 0 otherwise

1. Introduction

EXTREME weather conditions such as hurricanes are considered as high-impact low-probability (HILP) events, which have the potential to cause severe damage to the power system, resulting in major power outages and economic losses. More than 80% of power outages are caused by extreme weather-related disasters, with 90% of those occurring in the distribution network (DN) [1]. Therefore, it is crucial for the DN to have not only the ability to adapt to the varying operation conditions, but also the resilience to recover from disruptions rapidly. Two methods can be employed to enhance the resilience of DN: ① pre-fault measures such as network hardening typically demand significant investments of both money and time; ② post-fault measures such as network reconfiguration [2], microgrids [3], mobile energy sources [4], and novel power electronic devices [5], can leverage a variety of flexible resources to enable real-time management in the DN.

Soft open point (SOP) stands out as one of the most representative power electronic equipment, typically installed at normally open points [6]. Compared with traditional tie switch (TS), SOP provides continuous and accurate power and voltage regulations, offering substantial advantages to the DN. Under normal operating conditions, SOP functions by balancing load between feeders and improving voltage profile [7]. When a fault occurs, SOP can isolate the fault area and facilitate load transfer [8]-[10]. With the capability of voltage support, SOP contributes to establishing self-sufficient partitions, enabling rapid supply restoration and thus improving DN resilience. In addition, SOPs are frequently employed in coordination with dispatchable distributed generators (DGs) and remote switches during recovery process [11]-[13].

To maximize the recovery level of power customers, multiple SOPs are often deployed in a coordinated manner [14]. Determining the optimal siting and sizing of SOPs presents a challenging mixed-integer non-linear programming (MINLP) problem, often handled with heuristic algorithms [15]-[17]. However, heuristic algorithms do not guarantee global optimality and may fall into local optima. Reformulating the problems as mixed-integer linear programming (MILP) [18] or mixed-integer second-order cone programming (MISOCP) [19]-[23] makes it solvable with off-the-shelf solvers such as CPLEX [14], GUROBI [24] and MOSEK [25]. Considering the significant uncertainties associated with load demand and extreme weather, adopting a scenario-based stochastic programming (SBSP) formulation proves to be beneficial. Unlike robust optimization (RO), which tends to be over-conservative in the presence of HILP events, SBSP incorporates specific probability distributions, allowing for a balanced consideration of both normal and fault conditions. However, in large-scale SOP deployments involving multiple scenarios and time periods, extensive integer variables make it infeasible for commercial solvers to obtain exact solutions.

Given the inherent two-stage (investment and operation) structure of the planning problem, generalized Benders decomposition (GBD) [26] or column-and-constraint generation (C&CG) [19], [27] can be utilized to achieve global optimality. By decomposing the original problem into master problem and subproblems, it can be resolved in parallel across scenarios, thus enhancing the computational efficiency. However, standard dual theory cannot be applied to mixed-integer subproblems. Incorporating network reconfiguration constraints will make the classic GBD and C&CG algorithms impractical. To efficiently handle integer subproblems, some studies focus on deriving extended Benders cuts. Valid inequalities can be generated based on the convex hull representation of feasible region, using methods such as branch-and-bound [28] and cutting plane [29]. Nevertheless, two main challenges arise:

1) The Benders cuts may not hold for all values of first-stage variables, and can only be inherited from parent to child nodes during branching.

2) The cutting planes fail to provide sufficiently tight bounds for the relaxation of the subproblems, leading to computational inefficiency.

To address the above challenges, we propose a novel extreme weather risk-averse planning method for SOP based on Benders decomposition, which is designed to handle large-scale deployment problems involving numerous scenarios and integer variables. Table I compares the features of the proposed method with existing methods in the optimal operation and deployment of SOP.

TABLE I
COMPARISON OF FEATURES OF PROPOSED METHOD WITH EXISTING METHODS IN OPTIMAL OPERATION AND DEPLOYMENT OF SOP

Feature	Algorithm	Solution algorithm	Reference
Optimal operation of SOP	MILP	Auxiliary induce function (AIF)	[5]
	MINLP	Commercial solver	[8], [9]
	MINLP	Particle swarm optimization (PSO)	[30], [31]
	MILP	Iterative method	[12]
	SOCP or MISOCP	Commercial solver	[14], [25]
	Quadratic programming (QP)	Commercial solver	[32]
	RO, defender-attacker-defender (DAD)	Nested C&CG	[27]
Optimal deployment of SOP	MINLP	Archimedes optimization algorithm (AOA)	[15]
	MINLP	PSO	[16], [17]
	RO, MILP	Nested C&CG	[18]
	MISOCP	Iterative method	[19]
	MISOCP	Local search	[20]
	MISOCP	Commercial solver	[21], [24]
	RO, MISOCP	C&CG	[22], [33]
	MISOCP	GBD	This paper

The main contributions of this paper are threefold:

1) A two-stage SBSP model is developed for SOP planning considering extreme weather events. DN damage scenarios are generated from weather profiles and fragility curves. Network reconfiguration constraints are modified to support the islanded operation of SOPs and DGs.

2) A comprehensive objective function is formulated to minimize the investment and operational costs. Risk balancing between normal and fault scenarios is achieved by incorporating the CVaR of load shedding and network loss. The model is reformulated as an MISOCP problem with integer variables in both stages.

3) A novel GBD-based solution algorithm is developed to address large-scale instances with multiple scenarios. Lift-and-project (L&P) cuts are introduced to tighten the subproblems with integer constraints relaxed. An outer-approximation of SOCP constraints further improves the efficiency of generating the cutting plane.

The remainder of this paper is organized as follows. Section II introduces the preliminaries of the problem description. Section III establishes the two-stage SBSP model for SOP planning. Section IV proposes the GBD-based solution algorithm to solve the model. Case studies are carried out in Section V, and finally, Section VI concludes this paper.

II. PRELIMINARIES

This section provides the background on SOP operation and DN reconfiguration. In addition, the extreme scenario generation and reduction are introduced.

A. Problem Description

In this paper, we optimize the location and capacity of SOPs to reduce the operational costs and enhance the load restoration capability of the DN. SOPs are power electronic devices used to interconnect different AC feeders or buses. Common topologies include back-to-back (B2B) voltage source converters (VSCs) and multi-terminal VSCs [34]. This paper focuses on the B2B VSC configuration, where two VSCs are connected to a common DC bus. These converters are capable of controlling active power P, reactive power Q, DC voltage U_{dc}, AC voltage U_{ac}, and frequency f. Two typical control modes are considered: ① PQ-$U_{dc}Q$ mode, which regulates the active/reactive power between feeders during normal operation; ② $U_{ac}f$-$U_{dc}Q$ mode, which provides voltage support in isolated load islands after fault detection and isolation, with one terminal serving as the voltage reference.

The topology of DN is denoted by the graph $\mathcal{G}=\{\mathcal{N},\mathcal{B}\}$. $\mathcal{B}^{sop}$ may include existing tie lines to be replaced. It is assumed that renewable energy sources, e. g., wind and solar generators, are unavailable after a disaster; thus, only small synchronous generators with grid-forming converters are considered as controllable DGs for providing emergency support. The locations of these DGs are denoted as $\mathcal{N}^{dg}$. Nodes connecting the DN to the main grid are represented by $\mathcal{N}^{mg}$. In addition to $\mathcal{N}^{mg}$, nodes equipped with SOPs and DGs can also serve as the root bus of islands.

The strategy of network reconfiguration depends on the severity of faults. As shown in Fig. 1, during extreme weather events, multiple parts of the DN may be damaged, resulting in islands disconnected from any power source. We refer to these regions without active restoration ability as "completely isolated", whose restoration will be achieved by repair crews rather than SOPs. Given the set of outage branches $\mathcal{B}_{\omega}^{\text{out}}$ in scenario ω, the connected components of the subgraph formed by undamaged branches are identified before optimization. Components not connected to $\mathcal{N}^{\text{mg}}$, $\mathcal{N}^{\text{dg}}$, or $\mathcal{N}^{\text{sop}}$ are classified as isolated areas, denoted by sets of candidate SOP nodes $\mathcal{N}_{\omega}^{\text{iso}}$ and branches $\mathcal{B}_{\omega}^{\text{iso}}$. When both terminals of an SOP are connected to isolated nodes, as shown in Fig. 1(e), it cannot function properly as a voltage support.

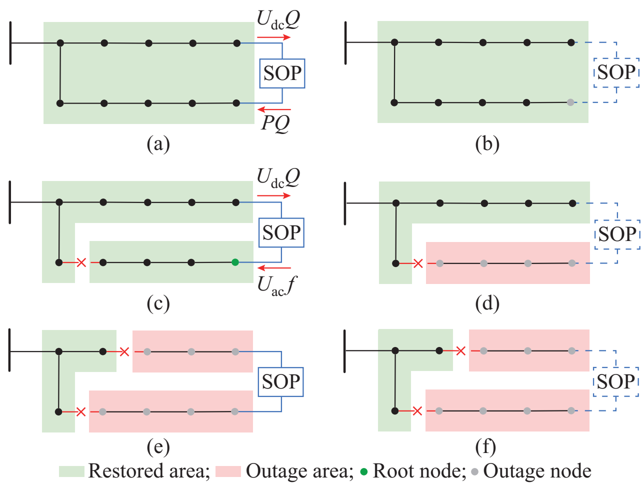

Fig. 1. Diagram of SOP function in no-damage, low-damage, and high-damage scenarios. (a) No-damage scenario with SOP. (b) No-damage scenario without SOP. (c) Low-damage scenario with SOP. (d) Low-damage scenario without SOP. (e) High-damage scenario with SOP. (f) High-damage scenario without SOP.

B. Scenario Generation and Reduction

The degree to which the scenario set approximates the original distribution significantly influences the outcomes of the SBSP. Accounting for the risk posed by extreme weather events on the DN, we employ Monte Carlo simulation to generate a series of scenarios. However, incorporating numerous scenarios results in the expansion of variables and parameters, thereby increasing the complexity of the two-stage SBSP model. To reduce the computational burden, we utilize clustering analysis to identify scenarios that best capture the impact of extreme weather. The schematic diagram of extreme scenario generation and reduction is depicted in Fig. 2.

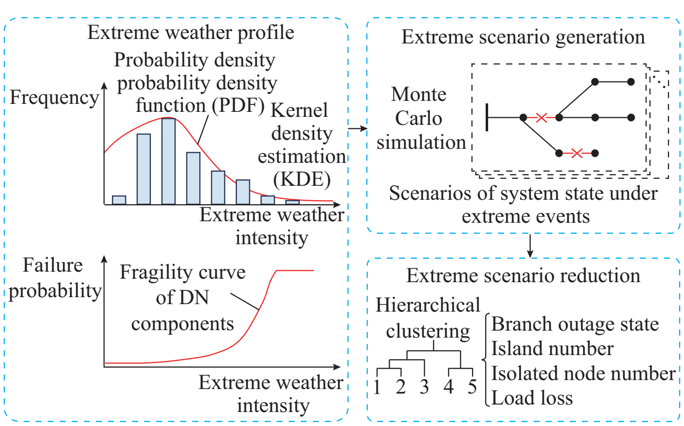

Fig. 2. Schematic diagram of extreme scenario generation and reduction.

The intensity of extreme weather can be reflected with weather parameters (e. g., wind speed for hurricanes) [35]. By analyzing the historical weather data, PDF of weather intensity is obtained by KDE. To assess the failure probability of components within the DN, a fragility function is introduced [36]. The fragility function of a distribution line across varying wind loadings can be expressed as:

$$p_{\text{fail}}(s)=\begin{cases} p_{\text{nm}} & s<s_{\text{cr}} \\ p_{\text{hw}}(s) & s_{\text{cr}}\leq s\leq s_{\text{co}} \\ 1 & s>s_{\text{co}} \end{cases} \tag{1}$$

Based on the extreme weather profile and fragility curve, the locations of outage branches in the DN are randomly sampled by Monte Carlo simulation. Furthermore, hierarchical clustering is conducted to retain the most critical scenarios while discarding redundant ones. Given that weather intensity typically follows a long-tail distribution, dividing scenarios into equal-sized clusters may result in ignoring HILP events. Therefore, in addition to the branch connection status $a_{ij,\omega}$, clustering features also encompass the number of islands, the number of isolated nodes, and the amount of load loss. Then, a distance-based method is used to identify the centroid of each cluster, thereby forming the representative scenario set Ω. The set of damaged branches $\mathcal{B}_{\omega}^{\text{out}}$ corresponding to each scenario $\omega\in\Omega$ is also identified. The probability of scenario p_{ω} is calculated as the ratio of the number of cluster to the total samples.

III. Two-Stage SBSP Model for SOP Planning

In this section, we establish a two-stage SBSP model for SOP planning. The model captures uncertainties related to extreme weather events through a finite set of representative scenarios Ω. The first stage focuses on determining suitable locations and capacities for SOPs to replace TSs, while the second stage optimizes the operating state of the DN in both normal and fault scenarios. The overall formulation is expressed as an MISOCP problem, minimizing the total costs including SOP investment cost, DN operational cost, and risks of load shedding and network loss.

A. Objective

1) SOP Investment Cost

$$C^{\text{inv}}=\pi^{\text{crf}}\sum_{(i,j)\in\mathcal{B}^{\text{sop}}}\left(x_{ij}^{\text{sop}}f_{ij}^{\text{sop, fi}}+S_{ij}^{\text{sop}}f_{ij}^{\text{sop, va}}\right) \tag{2}$$

$$\pi^{\text{crf}}=\frac{r(1+r)^{T}}{(1+r)^{T}-1}+m \tag{3}$$

where the capital recovery factor π^{crf} converts the present investment costs into a stream of equal annual payments during the planning horizon T.

2) DN Operational Costs and Risks of Load Shedding and Network Loss

$$C_{\omega}^{\text{ope}}=8760\left(Cost_{\omega}^{\text{dg}}+Cost_{\omega}^{\text{mg}}\right) \tag{4}$$

$$C_{\omega}^{\text{risk}}=8760\left(Cost_{\omega}^{\text{ls}}+Cost_{\omega}^{\text{nl}}\right) \tag{5}$$

Equation (4) defines the DN operational cost C_{ω}^{ope}, including DG generation cost $Cost_\omega^{dg}$ and electricity purchasing cost $Cost_\omega^{mg}$. Equation (5) introduces the risk costs $\mathcal{C}_\omega^{risk}$ associated with load shedding penalty $Cost_\omega^{ls}$ and network loss cost $Cost_\omega^{nl}$. The detailed expressions of each cost are given as:

$$\begin{cases} Cost_\omega^{dg} = \sum_{i \in \mathcal{N}^{dg}} \pi_i^{dg} P_{i,\omega}^{dg} \\ Cost_\omega^{mg} = \sum_{i \in \mathcal{N}^{mg}} \pi_\omega^{mg} P_{i,\omega}^{mg} \\ Cost_\omega^{ls} = \sum_{i \in \mathcal{N}} \pi^{ls} \left(1 - \lambda_{i,\omega}\right) w_i P_{i,\omega}^{d} \\ Cost_\omega^{nl} = \sum_{(i,j) \in \mathcal{B}} \pi^{nl} R_{ij} I_{ij,\omega}^{sq} \end{cases} \tag{6}$$

To strike a balance between costs and risks, we adopt conditional value-at-risk (CVaR) [37] as a metric to quantify extreme weather risks. It is defined by the expected costs in the worst $(1-\alpha)\cdot 100\%$ scenarios. The discrete convex form for CVaR minimization problem is given by [38]:

$$CVaR_\alpha = \eta + \frac{1}{1-\alpha} \sum_{\omega \in \Omega} p_\omega \left[\mathcal{C}_\omega^{risk} - \eta\right]_+ \tag{7}$$

The objective function is defined by the sum of annual investment cost $\mathcal{C}^{inv}$, expected operational cost $\mathbb{E}\left[\mathcal{C}_\omega^{ope}\right]$, expected risk cost $\mathbb{E}\left[\mathcal{C}_\omega^{risk}\right]$, and CVaR of risk cost $CVaR_\alpha$.

$$\begin{aligned} \min\left\{\mathcal{C}^{inv} + \mathbb{E}\left[\mathcal{C}_\omega^{ope}\right] + (1-\mu)\mathbb{E}\left[\mathcal{C}_\omega^{risk}\right] + \mu \cdot CVaR_\alpha\right\} = \\ \mathcal{C}^{inv} + \sum_{\omega \in \Omega} p_\omega \mathcal{C}_\omega^{ope} + (1-\mu) \sum_{\omega \in \Omega} p_\omega \mathcal{C}_\omega^{risk} + \mu \cdot CVaR_\alpha \end{aligned} \tag{8}$$

where $\mu \in [0,1]$. When μ takes a larger value, it indicates that the risk of failure in worst-case scenarios is given special attention, even if more investment is needed.

B. Constraints

1) Power Flow Constraints

$$\sum_{(i,j) \in \mathcal{B}} P_{ij,\omega} = \sum_{(j,i) \in \mathcal{B}} \left(P_{ji,\omega} - R_{ij} I_{ji,\omega}^{sq}\right) + P_{i,\omega} \tag{9}$$

$$\sum_{(i,j) \in \mathcal{B}} Q_{ij,\omega} = \sum_{(j,i) \in \mathcal{B}} \left(Q_{ji,\omega} - X_{ij} I_{ji,\omega}^{sq}\right) + Q_{i,\omega} \tag{10}$$

$$P_{i,\omega} = P_{i,\omega}^{mg} + P_{i,\omega}^{dg} + P_{i,\omega}^{sop} - \lambda_{i,\omega} P_{i,\omega}^{d} \tag{11}$$

$$Q_{i,\omega} = Q_{i,\omega}^{mg} + Q_{i,\omega}^{dg} + Q_{i,\omega}^{sop} - \lambda_{i,\omega} Q_{i,\omega}^{d} \tag{12}$$

$$\begin{aligned} \left|U_{i,\omega}^{sq} - U_{j,\omega}^{sq} + 2\left(R_{ij} P_{ji,\omega} + X_{ij} Q_{ji,\omega}\right) - \left(R_{ij}^2 + X_{ij}^2\right) I_{ji,\omega}^{sq}\right| \le \\ \left(1 - a_{ij,\omega}\right) M \end{aligned} \tag{13}$$

$$\left\| \begin{matrix} 2P_{ij,\omega} \\ 2Q_{ij,\omega} \\ I_{ij,\omega}^{sq} - U_{i,\omega}^{sq} \end{matrix} \right\|_2 \le I_{ij,\omega}^{sq} + U_{i,\omega}^{sq} \tag{14}$$

$$a_{ij,\omega} \in \{0,1\} \quad 0 \le \lambda_{i,\omega} \le 1 \tag{15}$$

Constraints (9)-(14) employ the DistFlow model to address the optimal power flow problem within a radial DN. Constraint (14) represents an SOCP relaxation of the non-linear power-voltage relationship, i.e., $P_{ij,\omega}^2 + Q_{ij,\omega}^2 = I_{ij,\omega}^2 U_{i,\omega}^2$. This relaxation has been proven to be exact under a sufficient condition for radial networks [39].

2) Network Security Constraints

$$U_{min}^2 \le U_{i,\omega}^{sq} \le U_{max}^2 \tag{16}$$

$$0 \le I_{ij,\omega}^{sq} \le a_{ij,\omega} I_{max}^2 \tag{17}$$

$$\begin{cases} -a_{ij,\omega} M \le P_{ij,\omega} \le a_{ij,\omega} M \\ -a_{ij,\omega} M \le Q_{ij,\omega} \le a_{ij,\omega} M \end{cases} \tag{18}$$

3) Network Reconfiguration Constraints

$$\sum_{(i,j) \in \mathcal{B}} a_{ij,\omega} = |\mathcal{N}| - \sum_{i \in \mathcal{N}} z_{i,\omega} \tag{19}$$

$$a_{ij,\omega} = b_{ij,\omega} + b_{ji,\omega} \quad \forall (i,j) \in \mathcal{B} \tag{20}$$

$$\sum_{(i,j) \in \mathcal{B}} b_{ij,\omega} = 1 - z_{i,\omega} \quad \forall i \in \mathcal{N} \tag{21}$$

$$\left|U_{i,\omega}^{sq} - 1\right| \le \left(1 - z_{i,\omega}\right) M \quad \forall i \in \mathcal{N}^{mg} \cup \mathcal{N}^{dg} \cup \mathcal{N}^{sop} \tag{22}$$

$$z_{i,\omega} = 1 \quad \forall i \in \mathcal{N}_\omega^{iso} \tag{23}$$

$$a_{ij,\omega} = 0 \quad \forall (i,j) \in \mathcal{B}_\omega^{out} \cup \mathcal{B}_\omega^{iso} \tag{24}$$

$$\sum_{(i,j) \in \mathcal{B} \setminus \left(\mathcal{B}_\omega^{out} \cup \mathcal{B}_\omega^{iso}\right)} \left|a_{ij,\omega} - a_{ij}^0\right| \le n_{ac} \tag{25}$$

$$z_{i,\omega} \in \{0,1\} \quad 0 \le b_{ij,\omega} \le 1, 0 \le b_{ji,\omega} \le 1 \tag{26}$$

Constraints (19)-(21) specify the radial network structure, while ensuring the connectivity within the islands formed. The value of $b_{ij,\omega}$ is already restricted to be 0 or 1 by (19)-(21), so it can be relaxed as continuous variables to improve the computational efficiency. Constraint (22) implies that root nodes have voltage support capability with the aid of grid-forming devices. In (23), the isolated nodes $\mathcal{B}_\omega^{iso}$ are specified as islands consisting of a single node. Constraint (25) limits the number of switch operations to be within n_{ac} during reconfiguration. Here, the TSs are assumed to be initially disconnected.

4) SOP Investment and Operation Constraints

$$x_{ij}^{sop} S_{min}^{sop} \le S_{ij}^{sop} \le x_{ij}^{sop} S_{max}^{sop} \tag{27}$$

$$\begin{cases} 0 \le S_{i,\omega}^{sop} \le S_{ij}^{sop} \\ 0 \le S_{j,\omega}^{sop} \le S_{ij}^{sop} \end{cases} \tag{28}$$

$$P_{i,\omega}^{sop} + \sigma_i^{sop} S_{i,\omega}^{sop} + P_{j,\omega}^{sop} + \sigma_j^{sop} S_{j,\omega}^{sop} = 0 \tag{29}$$

$$\begin{cases} \left\| P_{i,\omega}^{sop}, Q_{i,\omega}^{sop} \right\|_2 \le S_{i,\omega}^{sop} \\ \left\| P_{j,\omega}^{sop}, Q_{j,\omega}^{sop} \right\|_2 \le S_{j,\omega}^{sop} \end{cases} \tag{30}$$

$$a_{ij,\omega} \le 1 - x_{ij}^{sop} \quad \forall (i,j) \in \mathcal{B}^{sop} \tag{31}$$

$$z_{i,\omega} + z_{j,\omega} \le 1 \quad \forall i,j \notin \mathcal{N}_\omega^{iso}, (i,j) \in \mathcal{B}^{sop} \tag{32}$$

$$z_{i,\omega}, z_{j,\omega} \le x_{ij}^{sop} \quad \forall i,j \notin \mathcal{N}_\omega^{iso}, (i,j) \in \mathcal{B}^{sop} \tag{33}$$

Constraint (27) means that the SOP construction capacity S_{ij}^{sop} should be within the range of $\left[S_{min}^{sop}, S_{max}^{sop}\right]$. Constraints (28)-(30) give the relationship of power injection on both terminals i and j. Constraint (31) shows that the corresponding TS no longer works if replaced by SOP.

In addition, constraints (32) and (33) indicate that in $U_{\text{ac}}f$-$U_{\text{dc}}Q$ control mode, only one terminal of the VSCs can act as root node and provide voltage support for the island. If $z_{i,\omega}=0$ and $z_{j,\omega}=0$ on both terminals, the SOP works in PQ-$U_{\text{dc}}Q$ control mode and regulates the power between feeders.

5) DG Operation Constraints

$$0 \le P^{\text{dg}}_{i,\omega} \le P^{\text{dg}}_{\max,i} \tag{34}$$

$$Q^{\text{dg}}_{\min,i} \le Q^{\text{dg}}_{i,\omega} \le Q^{\text{dg}}_{\max,i} \tag{35}$$

$$-P^{\text{dg}}_{i,\omega}\tan\theta^{\text{dg}}_i \le Q^{\text{dg}}_{i,\omega} \le P^{\text{dg}}_{i,\omega}\tan\theta^{\text{dg}}_i \tag{36}$$

6) Main Grid Injection Constraints

$$0 \le P^{\text{mg}}_{i,\omega} \le P^{\text{mg}}_{\max} \quad \forall i \in \mathcal{N}^{\text{mg}} \tag{37}$$

$$0 \le Q^{\text{mg}}_{i,\omega} \le Q^{\text{mg}}_{\max} \quad \forall i \in \mathcal{N}^{\text{mg}} \tag{38}$$

C. Model Reformulation

Recalling the objective function (2)-(8) and constraints (9)-(38), the two-stage SBSP model for SOP planning can be reformulated into a two-stage MISOCP problem as:

$$\begin{cases} \min \left(\boldsymbol{f}^{\text{T}}\boldsymbol{X} + \sum\limits_{\omega\in\Omega} p_\omega \boldsymbol{g}^{\text{T}}_\omega \boldsymbol{Y}_\omega \right) \\ \text{s.t. } \boldsymbol{F}\boldsymbol{X} \le \boldsymbol{e} \\ \quad \left\| \boldsymbol{A}_{l,\omega}\boldsymbol{Y}_\omega + \boldsymbol{b}_{l,\omega} \right\|_2 \le \boldsymbol{c}^{\text{T}}_{l,\omega}\boldsymbol{Y}_\omega + \boldsymbol{d}^{\text{T}}_{l,\omega}\boldsymbol{X} \quad \forall l \\ \quad X_i \in \{0,1\} \quad \forall i \in \mathcal{I}_1 \\ \quad Y_{\omega,j} \in \{0,1\} \quad \forall j \in \mathcal{I}_2, \forall\omega \end{cases} \tag{39}$$

In (39), the linear constraints can also be transformed into SOCP form with $\boldsymbol{A}_{l,\omega}=\boldsymbol{0}$.

The variables in the first (investment) stage include:

$$\boldsymbol{X} = \left[\eta, x^{\text{sop}}_{ij}, S^{\text{sop}}_{ij} \right] \tag{40}$$

Besides, the variables in the second (operation) stage in scenario ω are the elements of the set:

$$\boldsymbol{Y}_\omega = \left[z_{i,\omega}, \lambda_{i,\omega}, P^{\text{mg}}_{i,\omega}, Q^{\text{mg}}_{i,\omega}, P^{\text{dg}}_{i,\omega}, Q^{\text{dg}}_{i,\omega}, P^{\text{sop}}_{i,\omega}, Q^{\text{sop}}_{i,\omega}, a_{ij,\omega}, b_{ij,\omega}, P_{ij,\omega}, Q_{ij,\omega}, U^{\text{sq}}_{i,\omega}, I^{\text{sq}}_{ij,\omega} \right] \tag{41}$$

The second-stage recourse problems are conditionally dependent on the decision of the first-stage variables $\boldsymbol{X}$, and hence cannot be directly decoupled across scenarios. Note that integer variables are present in both stages, i.e., x^{sop}_{ij} in the first stage and $z_{i,\omega}$ and $a_{ij,\omega}$ in the second stage, respectively.

IV. GBD-Based Solution Algorithm

GBD algorithm has been extensively used on combinatorial optimization. It decomposes the original problem into a master problem and multiple scenario-dependent subproblems, which can be solved in parallel to enhance the computational efficiency. However, with certain second-stage variables required to be integers, classic duality theory cannot be applied to generate standard Benders cuts. To address this, a GBD-based solution algorithm is proposed, as illustrated in Fig. 3. To further improve efficiency, we introduce the L&P cutting plane algorithm to derive strengthened Benders cuts through the convex hull of MISOCP subproblems.

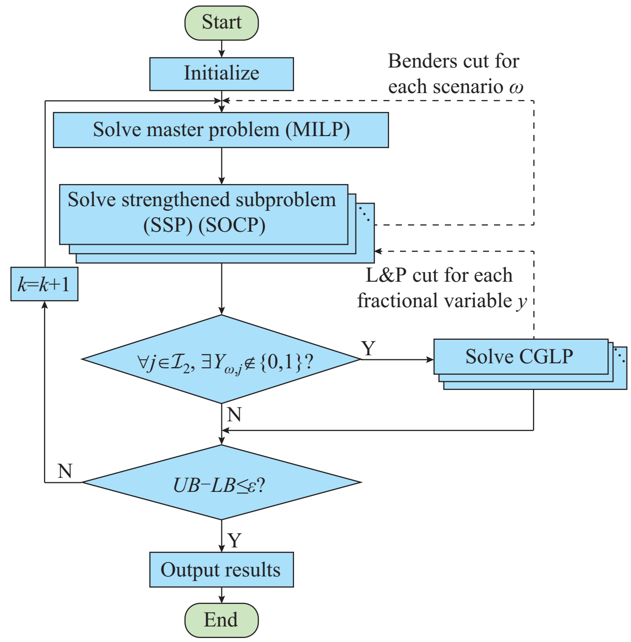

Fig. 3. Flowchart of proposed GBD-based solution algorithm.

A. Master Problem

The master problem at the k^{th} iteration is defined by (42) with the objective function z^{mp} and the optimal value of subproblem $\bar{z}^{\text{ssp}}_{\omega,k'}$:

$$\begin{cases} \min z^{\text{mp}}_k = \boldsymbol{f}^{\text{T}}\boldsymbol{X} + \sum\limits_{\omega\in\Omega} p_\omega \Phi_\omega \\ \text{s.t. } \boldsymbol{F}\boldsymbol{X} \le \boldsymbol{e} \\ \quad \Phi_\omega \ge \bar{z}^{\text{ssp}}_{\omega,k'} + \xi^{\eta}_{\omega,k'}\left(\eta - \bar{\eta}_{k'}\right) + \sum\limits_{(i,j)\in\mathcal{B}^{\text{sop}}} \xi^{x}_{ij,\omega,k'}\left(x^{\text{sop}}_{ij} - \bar{x}^{\text{sop}}_{ij,k'}\right) + \\ \quad \sum\limits_{(i,j)\in\mathcal{B}^{\text{sop}}} \xi^{S}_{ij,\omega,k'}\left(S^{\text{sop}}_{ij} - \bar{S}^{\text{sop}}_{ij,k'}\right) \quad \forall k' < k, \forall\omega \\ \quad X_i \in \{0,1\} \quad \forall i \in \mathcal{I}_1 \end{cases} \tag{42}$$

Constraint (42) is the Benders optimality cut, which is generated for each scenario ω at each iteration k. The parameters $\xi^{\eta}_{\omega,k'}$, $\xi^{x}_{ij,\omega,k'}$, and $\xi^{S}_{ij,\omega,k'}$ in the Benders cuts are the optimal dual variables related to $\boldsymbol{X}$, and are obtained by solving the Benders subproblems.

B. Benders Subproblems

When the first-stage variables are fixed at the optimal solution of the master problem, denoted as $\bar{\boldsymbol{X}} = \left[\bar{\eta}, \bar{x}^{\text{sop}}_{ij}, \bar{S}^{\text{sop}}_{ij} \right]$, the integer subproblems (ISPs) can be divided by scenarios as:

$$\begin{cases} \left(\text{ISP}_\omega\right): \min z^{\text{isp}}_{\omega,k} = \boldsymbol{g}^{\text{T}}_\omega \boldsymbol{Y}_\omega \\ \text{s.t. } \left\| \boldsymbol{A}_{l,\omega}\boldsymbol{Y}_\omega + \boldsymbol{b}_{l,\omega} \right\|_2 \le \boldsymbol{c}^{\text{T}}_{l,\omega}\boldsymbol{Y}_\omega + \boldsymbol{d}^{\text{T}}_{l,\omega}\boldsymbol{X} \quad \forall l \\ \quad \eta = \bar{\eta}_k \\ \quad x^{\text{sop}}_{ij} = \bar{x}^{\text{sop}}_{ij,k} \quad \forall (i,j) \in \mathcal{B}^{\text{sop}} \\ \quad S^{\text{sop}}_{ij} = \bar{S}^{\text{sop}}_{ij,k} \quad \forall (i,j) \in \mathcal{B}^{\text{sop}} \\ \quad Y_{\omega,j} \in \{0,1\} \quad \forall j \in \mathcal{I}_2 \end{cases} \tag{43}$$

Because of the integer constraint (the last constraint in (43)), it is not feasible to directly derive a valid Benders cut using dual theory. We firstly relax it into a continuous constraint (the last constraint in (44)). Then, the relaxed subproblem (RSP) is defined as:

$$\begin{cases} \left(\mathrm{RSP}_{\omega}\right): \min z_{\omega,k}^{\mathrm{rsp}} = \boldsymbol{g}_{\omega}^{\mathrm{T}} \boldsymbol{Y}_{\omega} \\ \text{s.t. Constraints in (43)} \\ \quad Y_{\omega,j} \in [0,1] \quad \forall j \in \mathcal{I}_2 \end{cases} \tag{44}$$

It should be noted that the relaxed subproblem will always be feasible given any SOP planning solution, as illustrated in the following proposition.

Proposition 1 (relatively complete recourse): for any first-stage solution $\bar{\boldsymbol{X}}$ satisfying constraint (42), if the DN satisfies $\left|\mathcal{B}^{\mathrm{sop}}\right| \ge \left|\mathcal{B}_{\omega}^{\mathrm{out}}\right|$, then the subproblem is feasible.

The proof of Proposition 1 is given in Supplementary Material A. In summary, for any MP solution $\bar{\boldsymbol{X}}$, there exists a feasible solution to the subproblem. The feasible region of relaxed subproblem is a subset of ISP_{ω}, and hence RSP_{ω} is also feasible. Then, Benders feasibility cuts are not necessary, which improves the computational efficiency of the iteration process.

C. Generation of L&P Cut

If the Benders cuts are derived directly from RSP_{ω} in (44), a looser feasible region will lead to a lower upper bound. To tighten the relaxation without imposing integer constraints, we introduce the rank-1 L&P cutting plane algorithm [40].

This algorithm constructs valid inequalities (VIs) by exploiting simple binary disjunctions. Given the optimal solution $\bar{Y}_{\omega}$ of RSP_{ω}, let $\mathcal{J}_{\omega,k} \subseteq \mathcal{I}_2$ denote the indices of 0-1 variables with fractional values. For variable $j \in \mathcal{J}_{\omega,k}$, the method introduces $Y_{\omega,j}$ and its complement to "lift" the RSP_{ω} into a higher-dimensional space. A valid cut is then generated by "projecting" it back, thereby eliminating the current fractional solution. A typical form of rank-1 disjunction is given as:

$$\mathcal{P} = \operatorname{conv}\left(\left\{\boldsymbol{e}_j^{\mathrm{T}} \boldsymbol{Y} \le 0\right\} \cup \left\{\boldsymbol{e}_j^{\mathrm{T}} \boldsymbol{Y} \ge 1\right\}\right) \tag{45}$$

where $\operatorname{conv}(\cdot)$ represents the convex hull. A unit vector $\boldsymbol{e}_j$ with the j^{th} element to be 1 serves as a splitting direction, similar in spirit to the branch-and-bound methods.

Reference [41] demonstrates that such cuts can be generated efficiently and are effective in reducing the integrity gap in MINLPs. Recognizing the complexity involved in solving non-linear programming (NLP) problems multiple times, we employ a polyhedral outer approximation of RSP_{ω} and convert the cut generating problem into a linear programming (LP) problem. The linearization process is given as:

$$\begin{aligned} &\nabla\left[\left\| \boldsymbol{A}_{l,\omega} \boldsymbol{Y}_{\omega} + \boldsymbol{b}_{l,\omega} \right\|_2 - \boldsymbol{c}_{l,\omega}^{\mathrm{T}} \boldsymbol{Y}_{\omega} - \boldsymbol{d}_{l,\omega}^{\mathrm{T}} \boldsymbol{X}\right]_o^{\mathrm{T}} \begin{bmatrix} \boldsymbol{X} - \hat{\boldsymbol{X}}^{(o)} \\ \boldsymbol{Y}_{\omega} - \hat{\boldsymbol{Y}}_{\omega}^{(o)} \end{bmatrix} = \\ &\left[\frac{\boldsymbol{A}_{l,\omega}^{\mathrm{T}}\left(\boldsymbol{A}_{l,\omega} \hat{\boldsymbol{Y}}_{\omega}^{(o)} + \boldsymbol{b}_{l,\omega}\right)}{\boldsymbol{A}_{l,\omega} \hat{\boldsymbol{Y}}_{\omega}^{(o)} + \boldsymbol{b}_{l,\omega}} - \boldsymbol{c}_{l,\omega}\right]^{\mathrm{T}} \left(\boldsymbol{Y}_{\omega} - \hat{\boldsymbol{Y}}_{\omega}^{(o)}\right) - \\ &\boldsymbol{d}_{l,\omega}^{\mathrm{T}}\left(\boldsymbol{X} - \hat{\boldsymbol{X}}^{(o)}\right) \le 0 \quad \forall o \end{aligned} \tag{46}$$

where $\left[\hat{\boldsymbol{X}}^{(o)}; \hat{\boldsymbol{Y}}_{\omega}^{(o)}\right]$ represents the sampled points used to construct the outerapproximation of the SOCP constraints in (43). The gradient term $\nabla[\cdot]_o$ corresponds to the normal vector at each point o, and the resulting linear inequality defines the tangent hyperplane at that location.

Specially, the nonlinearities in the problem arise from the SOCP constraints in (14) and (30), which geometrically correspond to a circle and a sphere, respectively. To construct the outerapproximation, we uniformly sample points along the boundaries of these geometric surfaces, and generate corresponding tangent hyperplanes. Let $\tilde{\boldsymbol{A}}\left[\boldsymbol{X}; \boldsymbol{Y}_{\omega}\right] \le \tilde{\boldsymbol{b}}$ denote the linear inequalities converted from the feasible region of RSP_{ω}. Then, rank-1 L&P cuts are generated by solving the following cut generating linear programming (CGLP) problem [42]:

$$\begin{cases} \left(\mathrm{CGLP}_{\omega j}\right): \min \left\{\beta - \boldsymbol{\alpha}^{\mathrm{T}} \begin{bmatrix} \bar{\boldsymbol{X}} \\ \bar{\boldsymbol{Y}}_{\omega} \end{bmatrix}\right\} \\ \text{s.t. } \boldsymbol{\alpha} = \tilde{\boldsymbol{A}}^{\mathrm{T}} \boldsymbol{u} + u_0 \boldsymbol{e}_j \\ \quad \boldsymbol{\alpha} = \tilde{\boldsymbol{A}}^{\mathrm{T}} \boldsymbol{v} - v_0 \boldsymbol{e}_j \\ \quad \beta = \tilde{\boldsymbol{b}}^{\mathrm{T}} \boldsymbol{u} \\ \quad \beta = \tilde{\boldsymbol{b}}^{\mathrm{T}} \boldsymbol{v} - v_0 \\ \quad \sum \boldsymbol{u} + \sum \boldsymbol{v} + u_0 + v_0 = 1 \\ \quad \boldsymbol{u}, \boldsymbol{v} \ge \boldsymbol{0} \\ \quad u_0, v_0 \ge 0 \end{cases} \tag{47}$$

where $\boldsymbol{\alpha}$, β, $\boldsymbol{u}$, $\boldsymbol{v}$, u_0, and v_0 are the newly introduced continuous variables. The optimal solutions of $\boldsymbol{\alpha}$ and β serve as the linear coefficients of the L&P cuts in (48). The generated L&P cuts are then added to the RSP_{ω} to strengthen its relaxation. The SSP is formulated as:

$$\begin{cases} \left(\mathrm{SSP}_{\omega}\right): \min z_{\omega,k}^{\mathrm{ssp}} = \boldsymbol{g}_{\omega}^{\mathrm{T}} \boldsymbol{Y}_{\omega} \\ \text{s.t. } \left\| \boldsymbol{A}_{l,\omega} \boldsymbol{Y}_{\omega} + \boldsymbol{b}_{l,\omega} \right\|_2 \le \boldsymbol{c}_{l,\omega}^{\mathrm{T}} \boldsymbol{Y}_{\omega} + \boldsymbol{d}_{l,\omega}^{\mathrm{T}} \boldsymbol{X} \quad \forall l \\ \quad \boldsymbol{\alpha}_{\omega,k',j}^{\mathrm{T}} \begin{bmatrix} \boldsymbol{X} \\ \boldsymbol{Y}_{\omega} \end{bmatrix} \le \beta_{\omega,k',j} \quad \forall k' \le k, \forall j \\ \quad \eta = \bar{\eta}_k : \xi_{\omega,k}^{\eta} \\ \quad x_{ij}^{\mathrm{sop}} = \bar{x}_{ij,k}^{\mathrm{sop}} : \xi_{ij,\omega,k}^{x} \quad \forall (i,j) \in \mathcal{B}^{\mathrm{sop}} \\ \quad S_{ij}^{\mathrm{sop}} = \bar{S}_{ij,k}^{\mathrm{sop}} : \xi_{ij,\omega,k}^{S} \quad \forall (i,j) \in \mathcal{B}^{\mathrm{sop}} \\ \quad Y_{\omega,j} \in [0,1] \quad \forall j \in \mathcal{I}_2 \end{cases} \tag{48}$$

where the dual variables $\xi_{\omega,k}^{\eta}$, $\xi_{ij,\omega,k}^{x}$, and $\xi_{ij,\omega,k}^{S}$ are associated with η, x_{ij}^{sop}, and S_{ij}^{sop}, respectively. Their optimal values are used as the coefficients in the Benders cut in (42).

Note that the outer approximation in (46) is only utilized for the generation of L&P cuts. SSP_{ω}, by contrast, is not further relaxed and retains the form of SOCP.

D. Implementation Procedure

The implementation procedure of the proposed GBD-based solution algorithm is summarized as follows.

Step 1: initialize $UB = \infty$ and $LB = -\infty$.

Step 2: at each iteration k, solve the master problem defined in (42) to obtain the first-stage variable $\bar{\boldsymbol{X}}$ and the current LB z_k^{mp}.

Step 3: for each scenario ω, solve the SSP_{ω} defined in (48) to obtain the second-stage variable $\bar{\boldsymbol{Y}}_{\omega}$.

Step 4: if any 0-1 variable j is fractional, solve the $\mathrm{CGLP}_{\omega j}$ defined in (47), and add the L&P cuts to SSP_{ω} by (48).

Step 5: solve the SSP_{ω} again to obtain the recourse cost $z_{\omega,k}^{\mathrm{ssp}}$ and dual variables $\xi_{\omega,k}^{\eta}$, $\xi_{ij,\omega,k}^{x}$, and $\xi_{ij,\omega,k}^{S}$.

Step 6: add the Benders cuts to MP by (42).

Step 7: repeat *Steps 2-6* until termination condition $UB-LB\leq\varepsilon$ is satisfied.

Notably, *Steps 3-6* are scenario-dependent and can therefore be executed in parallel to improve computational efficiency. In addition, the L&P cuts in (48) act as parametric cutting planes. Even though a single L&P cut may not be tight enough to restrict the fractional variables to integer values, they can accumulate over successive Benders iterations.

To illustrate the L&P generation procedure, we consider a numerical example involving an MINLP with two 0-1 variables, x and y, and a unique feasible solution at $(0,0)$. Figure 4 shows the schematic diagram of L&P cutting planes.

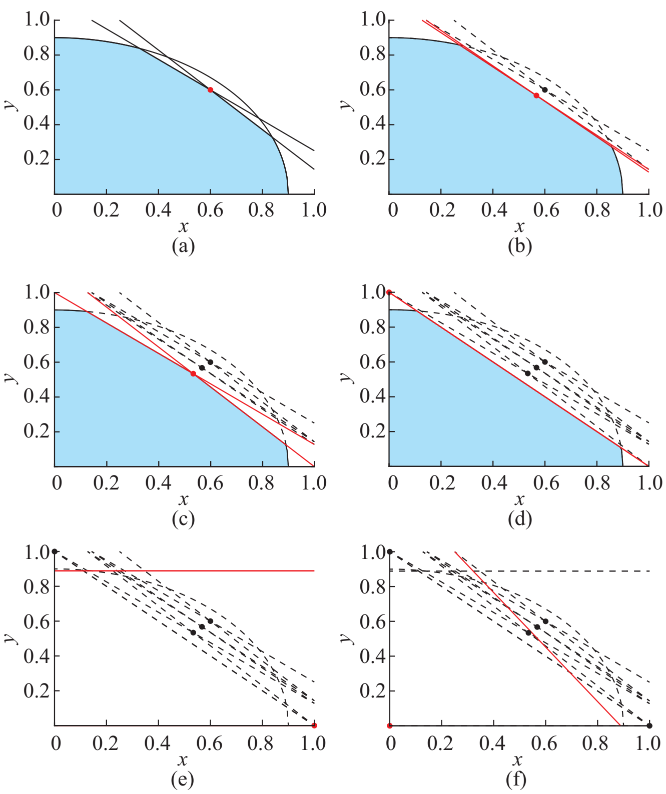

Fig. 4. Schematic diagram of L&P cutting planes. (a) $k=0$. (b) $k=1$. (c) $k=2$. (d) $k=3$. (e) $k=4$. (f) $k=5$.

The shaded area denotes the feasible region, the red lines are the L&P cuts for iteration k, and the black dashed lines are the invalid constraints. The black and red points denote the optimal value at each iteration and at previous iterations, respectively. The initial solution of the relaxed problem is $(0.60,\ 0.60)$, with both variables taking fractional values; thus, two L&P cuts are generated. After applying L&P cuts twice, the relaxed solution is tightened to $(0.57,\ 0.57)$ and then $(0.53, 0.53)$, as shown in Fig. 4(c) and (d), respectively. At iteration $k=3$, the solution $(0,1)$ violates the non-linear constraint, prompting the addition of a VI by outer approximation. This process repeats, and by $k=5$, the optimal solution converges to the integer solution $(0,0)$, as shown in Fig. 4(f).

V. Case Study

A. Parameter Settings

A modified 33-node DN [43] is employed to demonstrate the effectiveness of the proposed method, as shown in Fig. 5. The maximum active and reactive load demands are 3.71 MW and 2.30 Mvar, respectively. The load priority weights w_i are provided in Table II. Five tie lines in the DN serve as candidate locations for SOP installation. SOP construction capacity is limited between 400 and 200 kVA. Loss rates of SOP are 2% on both terminals. The fixed and variable costs of SOP are \$50000 and 100 \$/kVA, respectively. The system includes 6 DGs with a total capacity of 1.26 MW. Detailed parameters of the DGs are listed in Table III. Discount rate r and maintenance factor m are 5% and 2%, respectively, over a planning horizon T of 20 years. The resulting capital recovery factor is $\pi^{\mathrm{crf}}=0.1002$. The unit costs for load shedding and network loss are set to be \$5000 and 60 \$/MWh, respectively. The price of electricity purchased from the main grid is 60 \$/MWh. The maximum active and reactive power transmitted from the main grid, $P_{\max}^{\mathrm{mg}}$ and $Q_{\max}^{\mathrm{mg}}$, are 3 MW and 3 Mvar, respectively. The risk aversion coefficient is set to be $\mu=0.50$, and confidence level $\alpha=0.95$. The nodal voltage is limited within $[0.95, 1.05]$p.u..

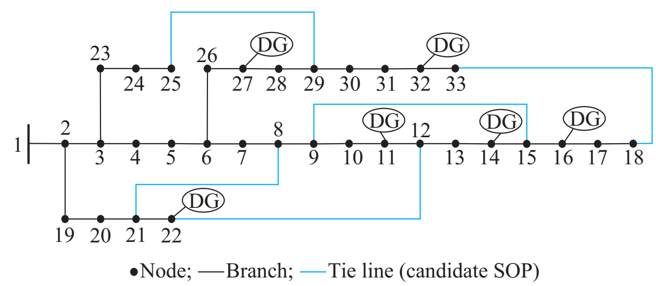

Fig. 5. Structure of modified 33-node DN.

TABLE II
LOAD PRIORITY WEIGHTS

Weight	Node
3	7, 8, 9, 10, 17, 18
2	11, 12, 13, 14, 15, 16, 19, 20, 21, 22
1	2, 3, 4, 5, 6, 23, 24, 25, 26, 27, 28, 29, 30, 31, 32, 33

TABLE III
DETAILED PARAMETERS OF DGs

Node	$P_{\max,i}^{\mathrm{dg}}$ (MW)	$Q_{\max,i}^{\mathrm{dg}}$ (MW)	$Q_{\min,i}^{\mathrm{dg}}$ (MW)	$\tan\theta_i^{\mathrm{dg}}$	π_i^{dg} (\$/MW)
11	0.22	0.22	−0.22	0.75	75
14	0.20	0.20	−0.18	0.75	80
16	0.18	0.18	−0.18	0.75	85
22	0.22	0.22	−0.22	0.75	75
28	0.26	0.26	−0.26	0.75	75
32	0.18	0.18	−0.18	0.75	80

In this paper, wind-related events such as typhoons and hurricanes are analyzed to assess their impact on the DN. Historical weather data from Shantou, China, spanning from 2019 to 2021, are utilized to estimate the PDF of wind speed by KDE. A representative scenario set Ω is generated by Monte Carlo simulation and reduced by hierarchical clustering, as described in Section II-B. The parameters of the fragility function in 1 are set as: $p_{\mathrm{nm}}=0.1\%$, $s_{\mathrm{cr}}=20$ m/s, and $s_{\mathrm{co}}=50$ m/s. The failure probability $p_{\mathrm{hw}}(s)$ increases exponentially with regard to the wind speed in the range of $\left[s_{\mathrm{cr}}, s_{\mathrm{co}}\right]$. Failures of nodes and tie lines are not considered in this paper. Figure 6 illustrates the scenario set Ω consisting of 13 scenarios, where red markers denote the locations of damaged branches $\mathcal{B}_{\omega}^{\mathrm{out}}$, the x-axis shows the from- and to-node of branches, and the y-axis shows the scenario index with its probability. For example, ω_1 (0.9429) represents the normal condition without any faults, with an occurrence probability of $p_{\omega_1}=94.29\%$. In scenario ω_{10}, a critical feeder $(2,3)$ near the common connection point is damaged. Scenario ω_{13} is also severely affected by the disaster, with 5 branches damaged. These severely impacted scenarios occur with low probability, e.g., $p_{\omega_{10}}=0.19\%$ and $p_{\omega_3}=0.29\%$.

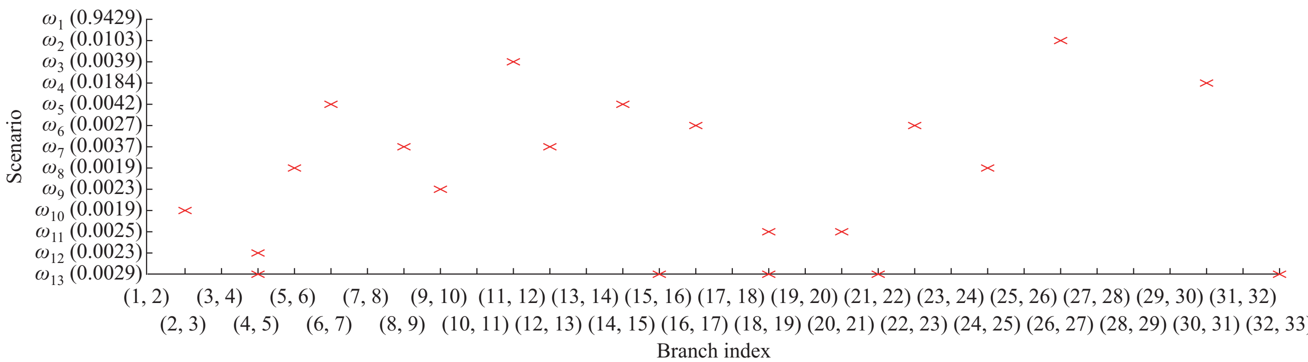

Fig. 6. Set of typical scenarios.

The SOP planning is optimized by the proposed GBD-based solution algorithm. GUROBI is utilized to solve the MISOCP and MILP problems, while MOSEK is used to solve the SOCP subproblems. Simulation is performed on a PC with Intel Core i7-12700 processor and 32 GB RAM. The tolerance gap for both the proposed GBD-based solution algorithm and solvers is set to be 0.001. It is noticed that numerical issues tend to arise during the generation process of L&P cuts, and hence result in the infeasibility of SSP_{ω}. To avoid this problem, inspired by [42], the rules are implemented as:

1) L&P cuts are generated for 0-1 variables $Y_{\omega,j}$ in SSP_{ω}, whose optimal value falls in the range of $[0.05, 0.95]$.

2) A cut is considered invalid if the optimal solution of α in $\mathrm{CGLP}_{\omega j}$ is larger than 0 but less than 1×10^{-6}.

3) A cut is considered invalid if the dual value of constraint (47) in $\mathrm{CGLP}_{\omega j}$ is less than 0.01.

B. SOP Planning Results

The proposed GBD-based solution algorithm converges at the 47th iteration, after running for 1892 s. According to the optimal solution, three of the five candidate SOPs are constructed to replace the TSs on branches $(9,15)$, $(12,22)$, and $(18,33)$. Capacities of each installed SOPs are 400 kVA, resulting in a total investment cost of \$270000. The expectations of annual operational cost $\mathbb{E}\left[\mathcal{C}_{\omega}^{\mathrm{ope}}\right]$ and risk cost $\mathbb{E}\left[\mathcal{C}_{\omega}^{\mathrm{risk}}\right]$ are 2.13 M\$ and 2.78 M\$, respectively. The CVaR of risk cost $CVaR_{\alpha}$ is 4.60 M\$.

According to the optimal solution $\boldsymbol{Y}_{\omega}^{*}$, the operation states for each scenario can be decided. The results of operation on modified 33-node DN are provided in Table IV, including the total active power of load shedding (load loss) $\sum\left(1-\lambda_{i,\omega}\right)P_{i,\omega}^{\mathrm{d}}$, network loss $\sum R_{ij}I_{ij,\omega}^{\mathrm{sq}}$, main grid injection $\sum P_{i,\omega}^{\mathrm{mg}}$, and power generation of DG $\sum P_{i,\omega}^{\mathrm{dg}}$. Significant differences are observed between the expectation and CVaR of load shedding and network loss. For example, scenarios ω_1-ω_5, which have fewer branches damaged and higher probability, exhibit the minimum load shedding. Conversely, scenario ω_{10}, where an outage occurs on a vital branch $(2,3)$, shows the highest the load shedding of 644 kW. In addition, given the higher unit cost of DG generation compared with the main grid transmission, the DN tends to utilize electricity from the main grid rather than utilizing DGs as emergency power sources.

TABLE IV
RESULTS OF OPERATION ON MODIFIED 33-NODE DN

Scenario index	Load loss (kW)	Network loss (kW)	Main grid injection (kW)	Power generation of DG (kW)
1	0.0	96.1	3000.0	830.0
2	12.7	123.1	2607.0	1260.0
3	0.0	101.9	2588.2	1260.0
4	0.0	116.8	2609.3	1260.0
5	0.0	101.8	2981.4	878.8
6	600.3	346.1	2245.0	1260.0
7	0.3	87.2	2576.5	1260.0
8	123.4	623.0	3000.0	1260.0
9	0.0	94.5	3000.0	843.3
10	644.0	1147.3	3000.0	1260.0
11	188.8	98.8	2394.4	1260.0
12	0.0	156.8	2652.8	1260.0
13	312.1	464.3	2634.8	1260.0
Expectation	4.6	101.7	2980.1	851.9
CVaR	91.9	208.4	3000.0	1260.0

Figure 7 illustrates the network configuration results of the modified 33-node DN in scenarios ω_{10} and ω_{13}. In scenario ω_{10}, the branch $(2,3)$ near the interconnection point with the main grid is damaged. To prevent voltage violations, load shedding occurs at nodes 24, 25, and 30. The voltage magnitude at node 23 drops to 0.951 p.u., which is close to the lower limit. SOPs play a critical role in maintaining power balance and improving voltage profile. For example, SOP2 injects 312 kW active power and 250 kvar reactive power at node 12. In scenario ω_{13}, as shown in Fig. 7 (b), three islands are formed after TS operations, e.g., node 22. It should be noted that node 33 experiences load shedding despite the support from DG at node 16 and SOP 3. This is because nodes 17 and 18 have the highest priority, with a total demand of 170 kW, while the maximum output capacity of DG 16 is 170 kW.

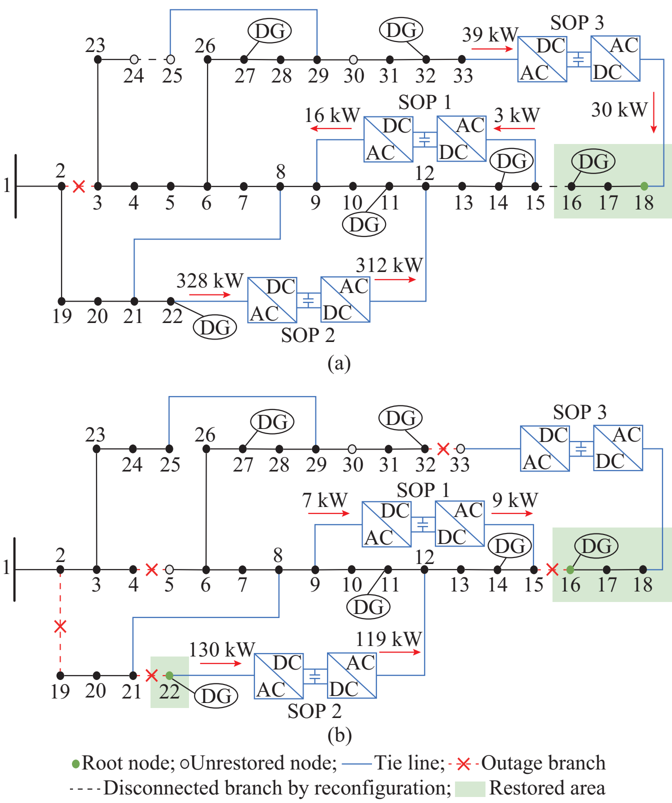

Fig. 7. Network configuration results of modified 33-node DN in scenarios ω_{10} and ω_{13}. (a) ω_{10}. (b) ω_{13}.

C. Performance of Proposed GBD-based Solution Algorithm

The iteration process of the proposed GBD-based solution algorithm is illustrated in Fig. 8, where the true upper bound derived from the integer subproblem ISP_ω (IUB) is $IUB = \boldsymbol{f}^{\mathrm{T}}\bar{\boldsymbol{X}} + \sum p_\omega z_{\omega,k}^{\mathrm{isp}}$. Due to the fact that finite L&P cuts are generally insufficient to tightly restrict the variables in SSP_ω to integer values, a gap may exist between the UB and the IUB. Once the algorithm converges to the optimal first-stage solution $\boldsymbol{X}^*$, the integer subproblems ISP_ω need to be re-solved to get the feasible second-stage decisions $\boldsymbol{Y}_\omega^*$.

Moreover, since L&P cuts are applied on the convex hull of the feasible region, the UB may increase instead of monotone decreasing, which is a significant difference from the classic GBD algorithm.

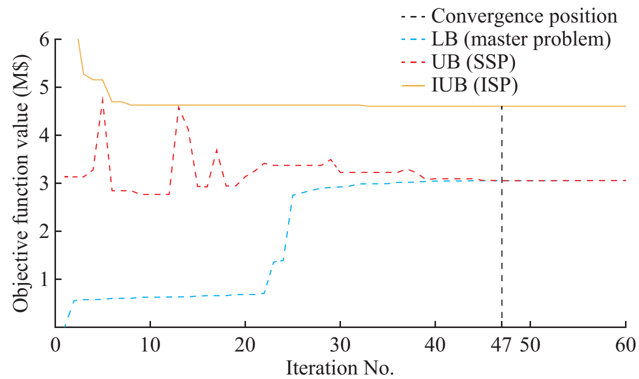

Fig. 8. Iteration process of proposed GBD-based solution algorithm.

To evaluate the efficiency and optimality of the proposed GBD-based solution algorithm, it is compared with GUROBI and genetic algorithm (GA). The original MISOCP problem in (39) is solved by GUROBI, with the minimum gap of 0.001. The solutions are considered as global optima. The first-stage variables $\boldsymbol{X}$ are optimized by GA Toolbox in MATLAB, and the subproblems ISP_ω are solved by GUROBI. The population size is set to be 10, the maximum generation number is set to be 50, the stall generation limit is set to be 10, and the crossover fraction is set to be 0.80.

All algorithms are computed in a pool with 8 parallel processes. Since GUROBI fails to solve the full case within a runtime of 30000 s (optimality gap is 27.9%), we reformulate three cases with fewer scenarios. The comparison results are given in Table V.

TABLE V
PERFORMANCE COMPARISON OF PROPOSED GBD-BASED SOLUTION ALGORITHM WITH OTHER ALGORITHMS

Case	$\lvert\Omega\rvert$	GUROBI		GA		Proposed	
		Time (s)	Objective (M$)	Time (s)	Objective (M$)	Time (s)	Objective (M$)
I	13			6268.5	4.679	1892.0	4.603
II	9	1814.8	3.643	2793.7	3.823	766.1	3.740
III	5	235.9	2.196	1880.6	2.200	148.4	2.207
IV	1	3.2	2.188	399.9	2.191	107.4	2.189

It can be observed that solution time of GUROBI increases significantly with the number of scenarios. The proposed GBD-based solution algorithm has a faster solving speed on large-scale instances. The optimality gaps are 2.66%, 0.51% and 0.04% for cases II-IV, respectively. While the outer approximation utilized in L&P cut generation may introduce a slight loss of accuracy, the resulting error remains within acceptable limits. In contrast, GA tends to converge to local optima, resulting in gaps of 4.94%, 0.50%, and 0.13% for the same cases. These results demonstrate that the proposed GBD-based solution algorithm is more efficient than the exact algorithm, and delivers higher-quality solutions than the heuristic algorithm.

D. Test on Large-scale DN

To evaluate the performance of the proposed method on a large-scale DN, a modified 123-node DN [22] with five substations and four DGs is utilized. The total rated active and reactive loads are 3.49 MW and 1.92 Mvar, respectively. Four DGs are located at nodes 27, 41, 85, and 110. Five candidate locations are considered for SOP installation: $(54,94)$, $(160,67)$, $(151,300)$, $(18,135)$, and $(48,250)$, among which the first three are divided whether to replace existing TSs. Load priorities are assumed to be identical across all nodes. All other parameter settings are consistent with the previous cases. After scenario generation, a total of 10 scenarios are obtained. The normal scenario ω_1 has a highest occurrence probability of 82.77%, and the most severe scenario ω_7 involves 20 damaged branches at a probability of only 0.07%.

The original MISOCP problem, with 50310 constraints and 27151 variables, is too complex for a direct solution using GUROBI. The proposed GBD-based solution algorithm converges at the 27$^{\text{th}}$ iteration within 1418 s, as shown in Fig. 9. The optimal planning results suggest installing an SOP at $(48,250)$ and replacing the TS with an SOP at $(151,300)$. The corresponding SOP capacities are 332.6 kVA and 400.0 kVA, respectively, leading to a total investment cost of \$173263. The results of operation on modified 123-node DN are summarized in Table VI.

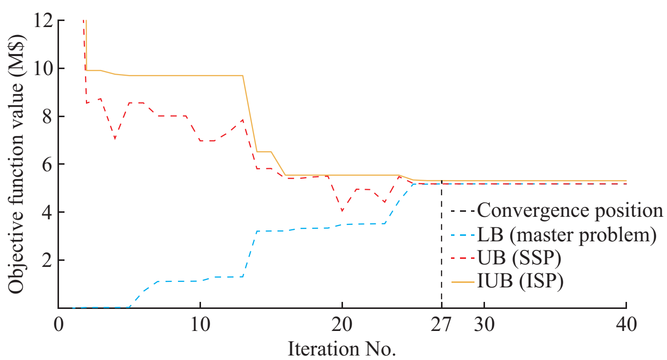

Fig. 9. Iteration process of proposed GBD-based solution algorithm on modified 123-node DN.

TABLE VI
RESULTS OF OPERATION ON MODIFIED 123-NODE DN

Scenario index	Load loss (kW)	Network loss (kW)	Main grid injection (kW)	Power generation of DG (kW)
1	0.0	82.8	2915.6	681.7
2	80.0	31.8	2955.6	508.2
3	60.0	102.2	3559.7	0.0
4	80.0	31.3	3250.0	215.8
5	810.0	14.9	2510.2	207.9
6	414.8	21.3	2641.3	480.2
7	675.0	26.3	2295.9	573.2
8	750.0	20.2	2371.0	409.2
9	720.0	25.9	2405.3	419.6
10	950.0	17.3	2350.0	224.8
Expectation	15.9	76.1	2941.2	633.2
CVaR	135.2	94.4	3373.4	681.7

The expected load shedding, CVaR, and maximum load shedding are 15.9 kW, 135.2 kW, and 950.0 kW, respectively. Notably, as the number of outage branches increases, the load loss tends to rise, indicating a significant impact of extreme events on system performance. In Fig. 10, scenario ω_8 is taken as an example to present the topology after reconfiguration. In this scenario, $\left|\mathcal{N}_\omega^{\text{iso}}\right|=16$ nodes including nodes 2, 11, and 19 become completely isolated. After TS operations, the DN is restructured into six separate islands, each represented by a different color. For example, DG at node 85 supports an island with load of 160.3 kW and 80.3 kvar. The total loss of load amounts to 750.0 kW, accounting for 21.5% of the overall system load. SOP 2 injects 319.3 kW active power and 93.1 kvar reactive power at terminal node 151, helping maintain its voltage at 0.988 p.u., even though it is far from the root node 195.

E. Sensitivity Analysis

1) Number of SOP Installations

To assess the impact of the number of SOP installations on operational performance, an addition constraint $\sum x_{ij}^{\text{sop}}=n_0$ is introduced into the MP, where n_0 varies from 0 to 5. The optimal number of SOP installations, i.e., $n_0=3$, has been identified in Section V-B. The sensitivity analysis results are given in Fig. 11. Note that different colored areas represent different restored areas. Due to the overall balance in power supply and demand, the operational cost $\mathbb{E}\left[\mathcal{C}_\omega^{\text{ope}}\right]$ remains relatively stable. However, the risk costs present a trend of first increasing and then decreasing. When the number of SOPs $n_0=0$, the absence of SOPs results in a high expected risk cost, due to insufficient voltage support. For example, the load at node 30 must be shed even in the normal scenario ω_1 due to voltage violations. Instead, installing an excessive number of SOPs (e.g., $n_0=5$) can also lead to a rise in $CVaR_\alpha$. This is because, in these cases, some TSs are replaced by SOPs, which may restrict the power transfer compared with the original tie lines. For example, if the TS $(8,21)$ in Fig. 7 is replaced by an SOP, downstream load will be significantly reduced due to the limited capacity of SOP.

2) Risk Aversion Coefficient

The impact of risk aversion coefficient μ, which controls the trade-off between $\mathbb{E}\left[\mathcal{C}_\omega^{\text{risk}}\right]$ and $CVaR_\alpha$, is examined. Interestingly, the variation of $\mu\in\{0.0,0.5,1.0\}$ does not change the number of SOP installations; however, it does influence their locations. The detailed analysis is given in Supplementary Material B.

VI. CONCLUSION

This paper presents an extreme weather risk-averse planning method for SOP. Representative scenarios are generated based on weather profiles and fragility curves, and a two-stage SBSP model is formulated to minimize the expectation and CVaR of load shedding and network loss. A novel GBD-based solution algorithm is proposed to address the integer and SOCP constraints. Tests on modified 33- and 123-node DNs confirm the effectiveness of the proposed method.

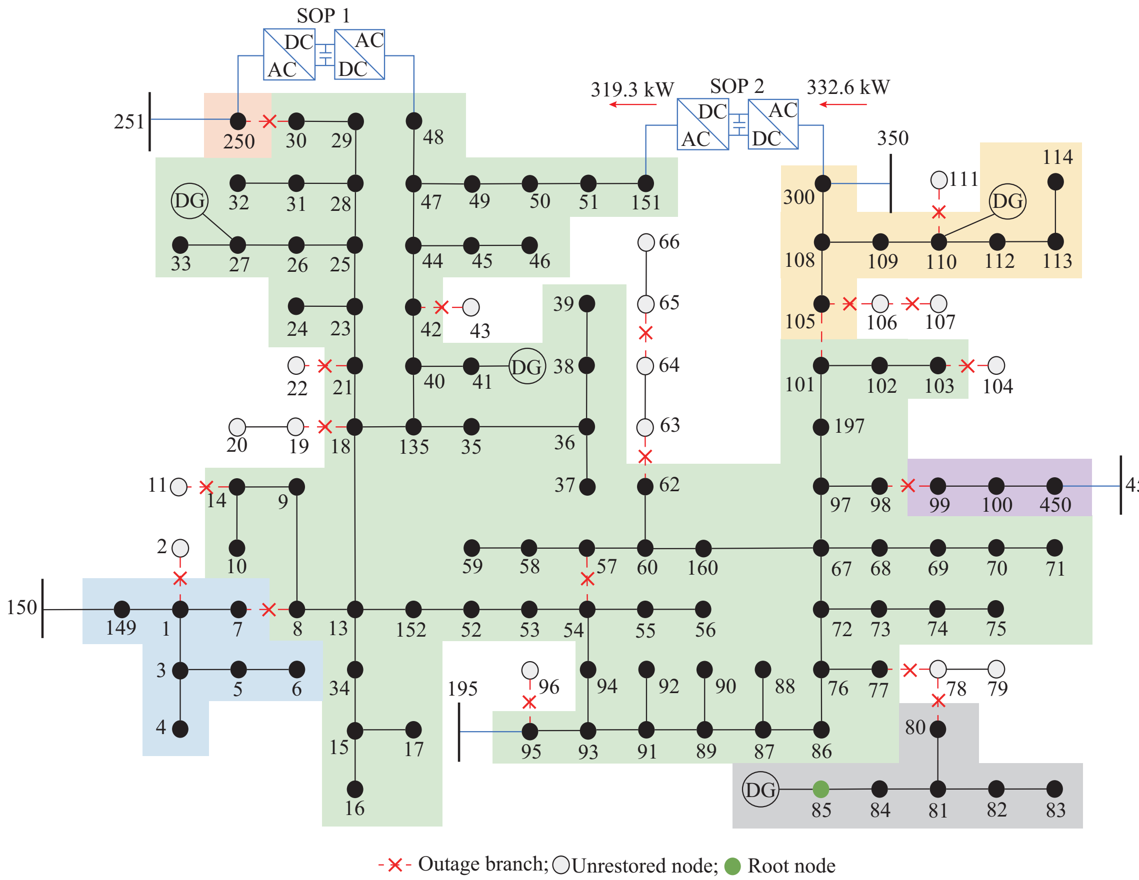

Fig. 10. Topology of modified 123-node DN in scenario ω_8.

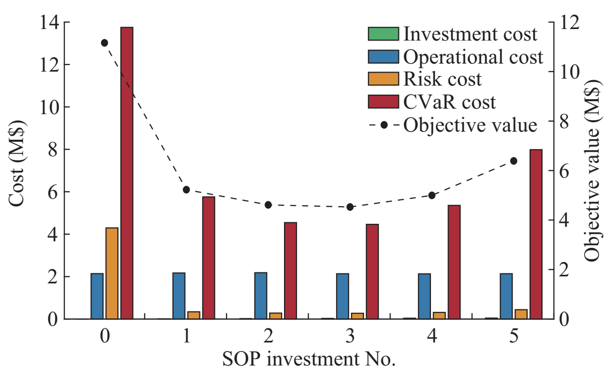

Fig. 11. Sensitivity analysis results.

For large-scale cases with multiple scenarios, the proposed GBD-based solution algorithm exhibits faster solution speed than GUROBI and GA, with optimality gaps of 2.66%, 0.51%, and 0.04% across different cases. Beyond SOP planning, the GBD-based solution algorithm also holds promise for other problems with mixed-integer convex problems, such as optimal power flow and unit commitment. Future work will explore the uncertainty in weather distributions and fragility models to enhance the robustness of the two-stage SBSP model.

REFERENCES

[1] N. L. Dehghani, A. B. Jeddi, and A. Shafieezadeh, "Intelligent hurricane resilience enhancement of power distribution systems via deep reinforcement learning," *Applied Energy*, vol. 285, p. 116355, Mar. 2021.
[2] J. Liu, C. Qin, and Y. Yu, "Enhancing distribution system resilience with proactive islanding and RCS-based fast fault isolation and service restoration," *IEEE Transactions on Smart Grid*, vol. 11, no. 3, pp. 2381-2395, May 2020.
[3] A. Hussain, V. H. Bui, and H. M. Kim, "Microgrids as a resilience resource and strategies used by microgrids for enhancing resilience," *Applied Energy*, vol. 240, pp. 56-72, Apr. 2019.
[4] S. Lei, C. Chen, Y. Li *et al.*, "Resilient disaster recovery logistics of distribution systems: co-optimize service restoration with repair crew and mobile power source dispatch," *IEEE Transactions on Smart Grid*, vol. 10, no. 6, pp. 6187-6202, Nov. 2019.
[5] T. Ding, Z. Wang, W. Jia *et al.*, "Multiperiod distribution system restoration with routing repair crews, mobile electric vehicles, and soft-open-point networked microgrids," *IEEE Transactions on Smart Grid*, vol. 11, no. 6, pp. 4795-4808, Nov. 2020.
[6] X. Jiang, Y. Zhou, W. Ming *et al.*, "An overview of soft open points in electricity distribution networks," *IEEE Transactions on Smart Grid*, vol. 13, no. 3, pp. 1899-1910, Feb. 2022.
[7] P. Li, H. Ji, C. Wang *et al.*, "Coordinated control method of voltage and reactive power for active distribution networks based on soft open point," *IEEE Transactions on Sustainable Energy*, vol. 8, no. 4, pp. 1430-1442, Oct. 2017.
[8] H. Ji, C. Wang, P. Li *et al.*, "SOP-based islanding partition method of active distribution networks considering the characteristics of DG, energy storage system and load," *Energy*, vol. 155, pp. 312-325, Jul. 2018.
[9] A. Escalera, M. Prodanović, E. D. Castronuovo *et al.*, "Contribution of active management technologies to the reliability of power distribution networks," *Applied Energy*, vol. 267, p. 114919, Jun. 2020.
[10] P. Fan, T. Yu, Z. Wang *et al.*, "Resilience-oriented soft open point deployment with topology-variable-based frequency stability constraints for distribution networks," *Applied Energy*, vol. 394, p. 126120, Sept. 2025.
[11] G. Zhang, F. Zhang, X. Zhang *et al.*, "Sequential disaster recovery model for distribution systems with co-optimization of maintenance and restoration crew dispatch," *IEEE Transactions on Smart Grid*, vol.

11, no. 6, pp. 4700-4713, Nov. 2020.
[12] T. Zhang, Y. Mu, L. Dong *et al*., "Fully parallel decentralized load restoration in coupled transmission and distribution system with soft open points," *Applied Energy*, vol. 349, p. 121626, Nov. 2023.
[13] G. Song, C. Ma, H. Ji *et al*., "Bi-level supply restoration method for active distribution networks considering multi-resource coordination," *Journal of Modern Power Systems and Clean Energy*, vol. 13, no. 3, pp. 967-979, May 2025.
[14] P. Li, J. Ji, H. Ji *et al*., "Self-healing oriented supply restoration method based on the coordination of multiple SOPs in active distribution networks," *Energy*, vol. 195, p. 116968, Mar. 2020.
[15] Z. M. Ali, I. M. Diaaeldin, A. El-Rafei *et al*., "A novel distributed generation planning algorithm via graphically-based network reconfiguration and soft open points placement using Archimedes optimization algorithm," *Ain Shams Engineering Journal*, vol. 12, no. 2, pp. 1923-1941, Jun. 2021.
[16] V. B. Pamshetti, S. Singh, A. K. Thakur *et al*., "Cooperative operational planning model for distributed energy resources with soft open point in active distribution network," *IEEE Transactions on Industry Applications*, vol. 59, no. 2, pp. 2140-2151, Mar. 2023.
[17] Q. Qin, B. Han, G. Li *et al*., "Capacity allocations of SOPs considering distribution network resilience through elastic models," *International Journal of Electrical Power & Energy Systems*, vol. 134, p. 107371, Jan. 2022.
[18] Z. Huang, Y. Zhang, and S. Xie, "A comprehensive strategy for the distribution network resilience enhancement considering the time-varying behaviors of typhoon path," *Electric Power Systems Research*, vol. 214, p. 108819, Jan. 2023.
[19] Y. He, H. Wu, R. Bi *et al*., "Coordinated planning of distributed generation and soft open points in active distribution network based on complete information dynamic game," *International Journal of Electrical Power & Energy Systems*, vol. 138, p. 107953, Jun. 2022.
[20] J. Zhang, A. Foley, and S. Wang, "Optimal planning of a soft open point in a distribution network subject to typhoons," *International Journal of Electrical Power & Energy Systems*, vol. 129, p. 106839, Jul. 2021.
[21] M. Ehsanbakhsh and M. S. Sepasian, "Bi-objective robust planning model for optimal allocation of soft open points in active distribution network: a flexibility improvement approach," *Electric Power Systems Research*, vol. 224, p. 109780, Nov. 2023.
[22] L. Ma, L. Wang, and Z. Liu, "Soft open points-assisted resilience enhancement of power distribution networks against cyber risks," *IEEE Transactions on Power Systems*, vol. 38, no. 1, pp. 31-41, Jan. 2023.
[23] X. Gong, K. Xie, C. Shao *et al*., "Post-disaster recovery of hybrid AC/DC cyber-physical distribution systems with adaptive switching of VSC control modes and scheduling of multi-type repair resources," *Journal of Modern Power Systems and Clean Energy*, doi: 10.35833/MPCE.2025.000145
[24] X. Yang, Z. Zhou, Y. Zhang *et al*., "Resilience-oriented co-deployment of remote- controlled switches and soft open points in distribution networks," *IEEE Transactions on Power Systems*, vol. 38, no. 2, pp. 1350-1365, Mar. 2023.
[25] C. Han, R. Rao, and S. Cho, "Stochastic operation of multi-terminal soft open points in distribution networks with distributionally robust chance-constrained optimization," in *Proceedings of 2025 IEEE PES General Meeting*, Austin, USA, Jul. 2025, pp. 1-6.
[26] R. Rahmaniani, T. G. Crainic, M. Gendreau *et al*., "The Benders decomposition algorithm: a literature review," *European Journal of Operational Research*, vol. 259, no. 3, pp. 801-817, Jun. 2017.
[27] X. Jing, W. Qin, H. Yao *et al*., "Resilience-oriented planning strategy for the cyber-physical ADN under malicious attacks," *Applied Energy*, vol. 353, p. 122052, Jan. 2024.
[28] S. A. Mansouri, A. Ahmarinejad, M. Ansarian *et al*., "Stochastic planning and operation of energy hubs considering demand response programs using Benders decomposition approach," *International Journal of Electrical Power & Energy Systems*, vol. 120, p. 106030, Sept. 2020.
[29] Y. Yin, T. Liu, L. Wu *et al*., "Frequency-constrained multi-source power system scheduling against $N-1$ contingency and renewable uncertainty," *Energy*, vol. 216, p. 119296, Feb. 2021.
[30] Q. Qi, J. Wu, and C. Long, "Multi-objective operation optimization of an electrical distribution network with soft open point," *Applied Energy*, vol. 208, pp. 734-744, Dec. 2017.
[31] L. Lan, G. Liu, S. Zhu *et al*., "Fault recovery strategy for urban distribution networks using soft open points," *Energy Conversion and Economics*, vol. 5, no. 1, pp. 42-53, Feb. 2024.
[32] X. Jiang, Y. Zhou, J. Wu *et al*., "Feasible operation region-based constraint management of distribution networks with soft open points," *IEEE Transactions on Power Systems*, vol. 40, no. 4, pp. 3160-3172, Jul. 2025.
[33] P. Cong, Z. Hu, W. Tang *et al*., "Optimal allocation of soft open points in active distribution network with high penetration of renewable energy generations," *IET Generation, Transmission & Distribution*, vol. 14, no. 26, pp. 6732-6740, Dec. 2020.
[34] X. Jiang, Y. Zhou, W. Ming *et al*., "An overview of soft open points in electricity distribution networks," *IEEE Transactions on Smart Grid*, vol. 13, no. 3, pp. 1899-1910, May 2022.
[35] M. Panteli, P. Mancarella, D. N. Trakas *et al*., "Metrics and quantification of operational and infrastructure resilience in power systems," *IEEE Transactions on Power Systems*, vol. 32, no. 6, pp. 4732-4742, Nov. 2017.
[36] M. Panteli, C. Pickering, S. Wilkinson *et al*., "Power system resilience to extreme weather: fragility modeling, probabilistic impact assessment, and adaptation measures," *IEEE Transactions on Power Systems*, vol. 32, no. 5, pp. 3747-3757, Sept. 2017.
[37] X. Duan, Z. Hu, and Y. Song, "Bidding strategies in energy and reserve markets for an aggregator of multiple EV fast charging stations with battery storage," *IEEE Transactions on Intelligent Transportation Systems*, vol. 22, no. 1, pp. 471-482, Jan. 2021.
[38] S. Moazeni, W. B. Powell, and A. H. Hajimiragha, "Mean-conditional value-at-risk optimal energy storage operation in the presence of transaction costs," *IEEE Transactions on Power Systems*, vol. 30, no. 3, pp. 1222-1232, May 2015.
[39] Z. Lin, Z. Hu, H. Zhang *et al*., "Optimal ESS allocation in distribution network using accelerated generalised Benders decomposition," *IET Generation, Transmission & Distribution*, vol. 13, no. 13, pp. 2738-2746, Jul. 2019.
[40] M. R. Kilinç, J. Linderoth, and J. Luedtke, "Lift-and-project cuts for convex mixed integer nonlinear programs," *Mathematical Programming Computation*, vol. 9, no. 4, pp. 499-526, Jan. 2017.
[41] C. Li and I. E. Grossmann, "An improved *L*-shaped method for two-stage convex 0-1 mixed integer nonlinear stochastic programs," *Computers & Chemical Engineering*, vol. 112, pp. 165-179, Apr. 2018.
[42] C. Li and I. E. Grossmann, "A generalized Benders decomposition-based branch and cut algorithm for two-stage stochastic programs with nonconvex constraints and mixed-binary first and second stage variables," *Journal of Global Optimization*, vol. 75, no. 2, pp. 247-272, Aug. 2019.
[43] C. Lee, C. Liu, S. Mehrotra *et al*., "Robust distribution network reconfiguration," *IEEE Transactions on Smart Grid*, vol. 6, no. 2, pp. 836-842, Mar. 2015.

Zhuoxu Chen received the B.S. degree in electrical engineering from Tsinghua University, Beijing, China, in 2022, where he is currently pursuing the Ph.D. degree in electrical engineering. His current research interests include electric vehicle and distribution system planning.

Zechun Hu received the B.S. and Ph.D. degrees in electrical engineering from Xi'an Jiao Tong University, Xi'an, China, in 2000 and 2006, respectively. He was with Shanghai Jiao Tong University, Shanghai, China, and also with the University of Bath, Bath, U.K., as a Research Officer from 2009 to 2010. He joined the Department of Electrical Engineering, Tsinghua University, Beijing, China, in 2010, where he is currently a Professor. His major research interests include optimal planning and operation of power system, electric vehicle, and energy storage system.

Yujian Wan is with the Shantou Power Supply Bureau of Guangdong Power Grid Corporation, Shantou, China, where he is currently a Senior Engineer. His major research interests include power system security analysis and management.

Junsong Li is with the Shantou Power Supply Bureau of Guangdong Power Grid Corporation, Shantou, China, where he is currently a Senior Engineer. His major research interests include power system security analysis and management.